Observations of Breaking Surface Wave Statistics

LI DING*

Department of Electrical and Computer Engineering, University of Victoria, Victoria, and Institute of Ocean Sciences, Sidney, British Columbia, Canada

DAVID M. FARMER

Institute of Ocean Sciences, Sidney, British Columbia, Canada

(Manuscript received 23 February 1993, in final form 20 October 1993)

ABSTRACT

Breaking surface waves were observed during the Surface Wave Processes Program with a novel acoustical instrument that makes use of underwater ambient sound to track individual breaking events. The spatial and temporal statistics of breaking waves such as duration, velocity, spacing, and breaking probability were determined under various wind and wave conditions. Statistical models are developed to assess and where appropriate, correct for any bias resulting from limitations of the measurement approach. Empirical relations of these statistics with wind speed are obtained. Comparison of the observed distributions with simultaneously measured directional wave spectra suggests that wave breaking occurs at multiple scales and that the mean scale of breaking is substantially smaller than the scale associated with the dominant wind wave component. Preliminary analysis indicates that the dependence of breaking probability on the fourth moment of the wave spectrum is consistent with a linear statistical model.

1. Introduction

Breaking surface waves are believed to play an important role in the dynamics of the upper ocean and air–sea interaction, contributing to surface wave dissipation (Melville and Rapp 1985; Agrawal et al. 1992) and enhancing the transfer of gas, heat, and mass across the ocean surface (Bortkovskii 1987; Thorpe 1992). While wave breaking has been the subject of both laboratory and theoretical studies (Phillips and Banner 1974; Longuet-Higgins and Fox 1977; Hwang et al. 1989), direct measurement of this phenomenon in the open ocean has been very limited. Especially important in this respect is measurement of the speed of breaking events, since this is related to the spectral scale at which wave breaking occurs and thus the scale at which dissipation due to breaking acts on the spectrum. Here we discuss measurements of various wave breaking properties obtained in the open ocean with a novel acoustical instrument.

The measurement principle involves tracking of discrete sound sources associated with breaking waves in both space and time as they travel across the ocean surface. In this sense our observations differ from point measurements, such as obtained by Thorpe and Humpheries (1980), Longuet-Higgins and Smith (1983), and Hwang et al. (1989). Our observations also differ from integral descriptions, in particular observations of whitecap coverage (Monahan and O'Muirhearataigh 1986), which is an indirect measure of breaking waves and not so readily interpreted in terms of dynamical properties of waves. Photographic measurements of discrete whitecaps have also been acquired in a fetch limited sea by Snyder et al. (1983), who were able to measure spatial and temporal scales of whitecaps. However, their observation area was rather limited (10 m × 10 m), and it was often difficult to collect sufficient breaking events for statistical analysis.

Sound generated by breaking waves provides an opportunity for remote measurement of the wave breaking process, and a series of laboratory and field experiments have thus been designed to test the feasibility of this approach. Farmer and Vagle (1988) observed ambient sound with a single hydrophone and found that the variability of sound spectrum levels can be related to the temporal group structure of wave breaking (Donelan et al. 1972). Crowther and Hansla (1993) used an array of narrow-beam, high-frequency sonars (10–50 kHz) to track breaking waves in a fetch-limited sea. In the laboratory, the acoustic power radiated by a breaking wave has been found to be proportional to the dissipated mechanical energy due to breaking

* Current affiliation: Marine Physical Laboratory, Scripps Institution of Oceanography, University of California, San Diego, California.

Corresponding author address: Dr. David M. Farmer, Institute of Ocean Sciences, P.O. Box 6000, 9860 West Saanich Road, Sidney, BC V8L 4B2, Canada.

(Melville et al. 1988), implying that the dynamical properties of breaking waves could also be acoustically probed.

In this paper, we present the statistics of breaking surface waves in the open ocean measured with a hydrophone array. These statistics, including breaking event density, duration, and velocity, represent some fundamental spatial and temporal characteristics of breaking waves. We shall first describe the experiment and technology, and then perform a statistical analysis of the experimental results. The statistics are obtained under various meteorological conditions and compared with simultaneously measured directional wave spectra. Conclusions are drawn from these observations concerning the scale of breaking, its directionality and relationship to the wave field parameters.

2. Experiment and technology

Our observations of ambient sound were conducted as part of the SWAPP (Surface Wave Processes Program) experiment, about 600 miles WNW of San Diego (35°N, 127°W), in February/March 1990. The experiment included the RP *FLIP* and Canadian vessel CSS *Parizeau* from which we deployed a self-contained and freely drifting hydrophone array. The array was suspended at 25 m and used to track local breaking waves. Two types of wave data were acquired from RP *FLIP* and kindly made available to us by Dr. J. Smith (Scripps Institution of Oceanography). These included one-dimensional wave spectra measured with a capacitance wave gauge, and directional wave spectra inferred from nearly horizontally oriented Doppler sonars. Standard meteorological measurements were also made from *FLIP* and *Parizeau*.

The technical approach used to track breaking waves has been discussed by Ding and Farmer (1992a), but is summarized here for convenience. We used an array of four hydrophones of span 8.5 m and bandwidth 5.5 kHz[1] to measure ambient sound. The data were digitized at 11 kHz and stored on videotapes for processing. The depth and orientation of the array were simultaneously measured. Acoustic signals from breaking waves arriving at different hydrophones are cross correlated to determine time delays. Given the geometry of the array and the time delays, breaking events at the surface can be located. Cross correlations are calculated at each successive time step, and a series of correlations allows us to construct a two-dimensional image. Figure 1 shows correlation images for a typical event from four hydrophone pairs, where the horizontal axis, vertical axis, and gray level (or color) represent time, time delay, and correlation level, respectively. Additional correlation images can be found in Ding and Farmer (1992a), Farmer and Ding (1992), and Ding (1993). The dark streaks correspond to higher correlations and are associated with the breaking events as they move across the ocean surface. Such patterns in the correlation image are extracted to track individual breaking waves by taking into account the array geometry and depth. As discussed in detail by Ding and Farmer (1992a), the procedure for tracking breaking waves in space and time is carried out automatically using a pattern recognition scheme.

Farmer and Ding (1992) show that a breaking wave cannot be treated as a compact acoustic source if the hydrophone array is sufficiently close to the source that the source size, as viewed from the array, cannot be neglected for the available acoustic bandwidth. The finite size of a source reduces the spatial coherence of radiated signals received at the array. Since the spatial dimension of a breaking wave is anisotropic, with the crosswind dimension typically being longer than the downwind dimension, correlation images obtained from different hydrophone pairs also show anisotropy. For example, it can be seen in Fig. 1 that the streaks on hydrophone pairs 2–1 and 3–1 are more clear and last for a longer period than on the other two pairs. The first two pairs are therefore automatically selected in the pattern recognition scheme to track the event. There are, however, some events that can only be identified on one hydrophone pair. We refer to this as the finite source dimension effect. Possible effects of finite source dimension on measurement results are carefully examined later.

Due to background noise and the simplicity of the array, the detection area is limited (of radius 40 m) and only relatively large breaking waves can be detected. A statistical model is developed to allow correction for loss of small events. Occasionally, two events will occur simultaneously within the detection area. For well-separated events, this leads to a second peak in the correlation function and is readily discerned in the correlation image. If on the other hand, the events are too close together throughout their lifetime, the correlation peaks may not be separable. In this case however the breaking events are likely to be dynamically related and it seems reasonable to treat them as a single event. Because of the limited detection area and relatively large scales of detected events, multiple events rarely occurred simultaneously in our data and no attempt was made to assess the ability to separate them with the present instrument. Discrimination at this end would require a much more elaborate hydrophone array.

3. Statistical analysis

The hydrophone array detects sound radiated from individual breaking events. However, as indicated

[1] The choice of this bandwidth was primarily due to computational and instrumental limits. The instrument was designed for more comprehensive measurement of near-surface processes, and part of the recording capacity had to be allocated to active sonar. It was later realized that for frequencies higher than 2.5 kHz, ambient sound is essentially incoherent over the hydrophone spacing (Farmer and Ding 1992) and does not contribute to tracking of breaking waves.

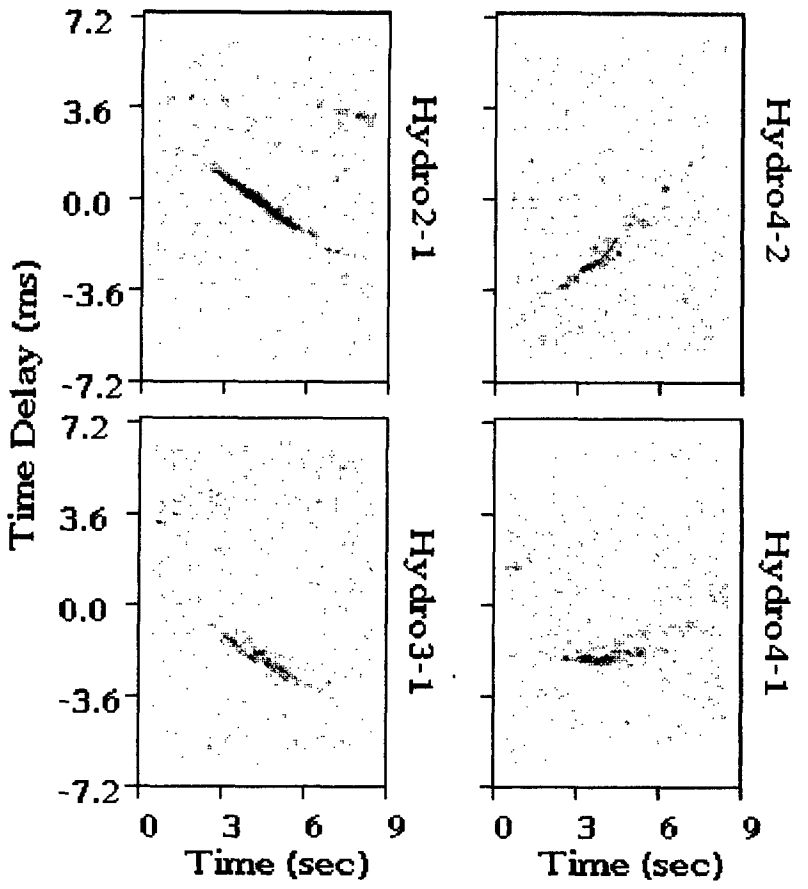

FIG. 1. Correlation images for a typical breaking wave from four different hydrophone pairs. The horizontal axis is time and the vertical axis is time delay between hydrophones. Dark streaks correspond to high correlation associated with the breaking event. Hydrophone pairs 2–1 and 3–1 show higher correlation than the other two, and are chosen for tracking the breaking event.

above, the source locations can only be determined if the signal rises above the background noise field, and if in addition, it is coherent across the hydrophone array. Whether or not a particular wave is detectable in a given noise field depends on the source strength, acoustical radiation pattern and range. Similarly, the near-field problem that reduces the coherence of a source depends on its dimension, orientation, and range. Care is required to allow for these effects. The statistical analysis in this section involves two aspects: determination of thresholds used to separate breaking events from background noise and assessment of, and corrections for, the effects of background noise and finite source dimension.

a. Determination of thresholds

The event identification scheme described in Ding and Farmer (1992a) selects from the correlation image those events with correlation strength above some threshold. The determination of this threshold is important to the later statistical analysis, since too high a value leads to needless elimination of events whereas too low a value introduces too much noise. Therefore we must choose this threshold optimally in some statistical sense.

If events are well separated from background, then their statistical properties, such as their probability distributions of correlation strength, should be sufficiently different. Let x be a random variable representing the correlation level of events and y be that of background noise. Assume that the probability of selecting events is p. Then the selected correlation level, z, is given by

$$z = \begin{cases} x & \text{with probability } p \\ y & \text{with probability } 1 - p. \end{cases}$$

This yields a distribution of z

$$f_z(z) = pf_x(z) + (1 - p)f_y(z), \qquad (1)$$

where $f_x(x)$ and $f_y(y)$ are the probability density functions of x and y, respectively (see Papoulis 1984, p. 84).

Figure 2 shows a sketch of $f_x(z)$, $f_y(z)$, and $f_z(z)$. It can be seen that $f_z(z)$ has two maxima, with one corresponding to $f_x(z)$ and the other to $f_y(z)$. A threshold lies between these two maxima. The optimal choice of the threshold should be the local minimum (z_c) between the two distributions.

The correlation image is digitized to 16 levels and then searched for event patterns with correlation over some threshold. The density distribution of events is thus obtained. Figure 3a shows the number of identified events at different correlation levels (from dataset 3 in Table 1). We choose the minimum at level $G = 3$ as a threshold. Considering all the datasets, $G = 3$ is typical at high winds (>7 m s^{-1}) while $G = 4$ is selected at lower winds (<7 m s^{-1}).

In addition to the correlation threshold, it is also necessary to determine the minimum size of breaking waves so as to separate breaking events from nonspecific variability in the sound field. One apparent parameter is duration. In other words, we need to impose a short duration cutoff to reduce further noise lying above the correlation threshold. The same procedure can also be used to choose the duration threshold. Figure 3b shows the number of events at different durations with correlation over the selected threshold, where it can be seen that $D = 4$ (samples) is the optimal choice for the duration threshold, since it appears to separate a smoothly varying distribution from a much larger number of short events, which are identified as noise. This choice is typical of the data we have analyzed, though for some datasets $D = 5$ was chosen.

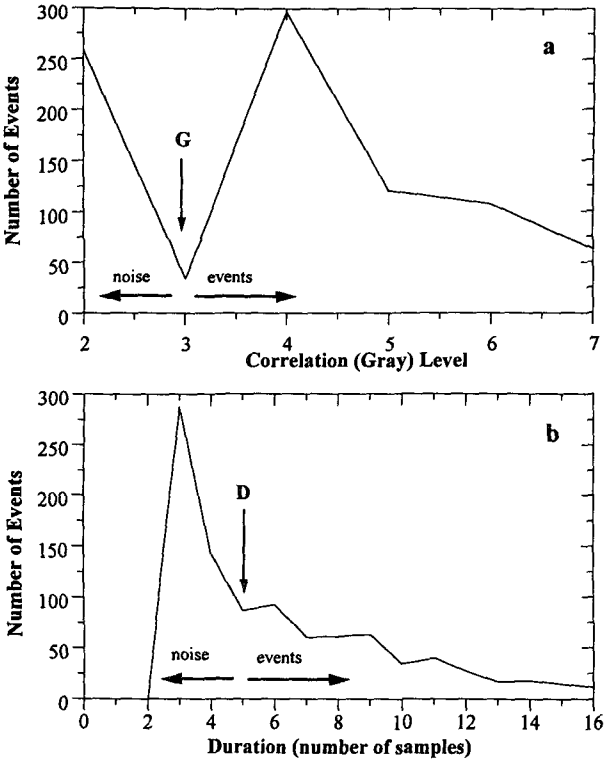

FIG. 3. Determination of correlation level and duration thresholds. (a) Density distribution of events with respect to correlation level, where the level threshold is chosen at $G = 3$. (b) Density distribution with respect to duration for events with correlation level above the selected threshold. The duration threshold is at $D = 4$ samples (corresponding to 0.34 s).

b. *Incomplete measurement and correction*

By incomplete measurement, we mean that the instrument cannot measure all the events that actually occur. Incomplete measurement is caused by two factors. One is background noise; weak events cannot be detected if their signal to noise ratios (SNR) are below a certain threshold. This also results in a position dependence of the measured breaking duration. The second factor is the finite source dimension effect mentioned earlier. Incomplete measurement biases the resulting statistics, and thus must be corrected to some extent. To explain the problem conveniently, we define the following concepts:

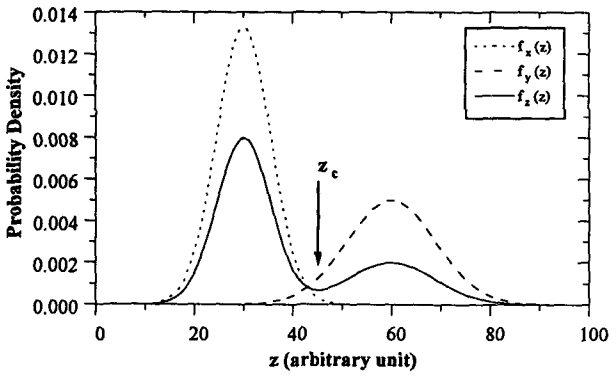

FIG. 2. Illustrative sketch of the probability distribution (in arbitrary units) in a two-mode model, where z_c is the selected threshold; $f_z(z)$ is shown as the solid line.

Detectability: An event is detectable if it can be seen on any hydrophone pair.

Locatability: An event is locatable if it can be seen on more than one hydrophone pair.

Trackability: An event is trackable if it can be seen on more than one hydrophone pair and its duration is long enough that its motion can be tracked.

1) DETECTABILITY

Detectability is determined by received signal intensity, background noise, and the required SNR threshold for detection. Received intensity depends on the acoustic strength of a breaking wave and the distance from the wave to the array. Background noise depends on the environment and the required SNR threshold is fixed once the event detection algorithm is chosen.

Detectability of events is described in terms of detection probability, which is derived in appendix A.

One of the important breaking wave parameters is event density, that is, the number of events in a unit area. It is shown in appendix D that the number of events in a selected area can be derived from the number of detectable events in the area and the detection probability.

2) CORRECTION OF DURATION

Because of the background noise, the breaking duration measured from the correlation image is dependent on the event position. That is, a distant event "looks" shorter than a local one even if they have equal durations, because the intensity detected for the distant event is weaker. A maximum likelihood (ML) estimator has thus been developed to correct the measured duration for the range dependence, the details of which are given in appendix B.

3) LOCATABILITY AND TRACKABILITY

Determination of event density requires determination of the number of detectable events in an "observation" area within the detection area. However, due to the finite source dimension effect, some of these detectable events may not be locatable. Nevertheless, from the correlation images, we can determine the ratio of the number of locatable events to that of detectable events within the detection area, which will be called the "locatability ratio." This ratio, however, will be used in the observation area, which is enclosed by the detection area, since most of the lost events due to the finite source dimension effect are expected to be relatively close to the hydrophone array. More distant events would subtend a smaller angle and thus be more readily locatable if they rise above the background noise. The locatability ratio obtained in an observation area can thus be considered approximately equal to the ratio obtained in the detection area. Therefore, the number of detectable events in the observation area is obtained from the number of locatable events and the locatability ratio.

Trackability is equivalent to locatability except that it requires a longer duration for tracking. Therefore, events with observed durations shorter than a threshold cannot be tracked. In addition, if the event is too far away, it may not be possible to track it due to larger tracking errors occurring at greater distance. The proportion of trackable events is normally 80% of locatable events.

c. *Effects of incomplete measurement on the distribution of breaking parameters*

Incomplete measurement not only leads to an underestimate of the total number of events but may also affect the overall distribution of breaking parameters. Here we discuss the possible effects of incomplete measurement on the distributions of two parameters: event speed and duration.

1) BACKGROUND NOISE

Consider first the effect of background noise. To model its effect, we assume that the background noise results mainly from the contributions of breaking waves randomly and uniformly distributed at the ocean surface. It is recognized that there may be some process, for example, modulation of surface waves by Langmuir circulation, that could introduce a nonrandom influence on the spatial distribution of breaking. To examine this problem, we show in Fig. 4 the locations of detected breaking events superimposed for a period of 30 min (using dataset 22), where no obvious departure from uniformity is seen to emerge. However, it must be recognized that over this 30-min period, it is most unlikely that a stationary pattern of circulation would exist around the instrument. In the absence of simultaneous measurements of the local flow variability it is not possible to assert unequivocally that the spatial distribution of breaking is truly random. Nevertheless, given the available information, this assumption seems reasonable and we proceed on this basis to derive a model to evaluate the effect of noise (see appendix C). It is shown that background noise masks small-scale breaking events and therefore affects the distributions at lower values. It imposes a small-scale cutoff on our measurements of breaking waves. For example, the lowest event speed and shortest duration detectable in dataset 3 (Table 1), which was collected at a wind speed of 9.9 m s^{-1}, are estimated in appendix C to be 1.8 m s^{-1} and 0.5 s.

2) FINITE SOURCE DIMENSION

Finite source dimension may also affect the calculated distribution of breaking parameters. Figure 5

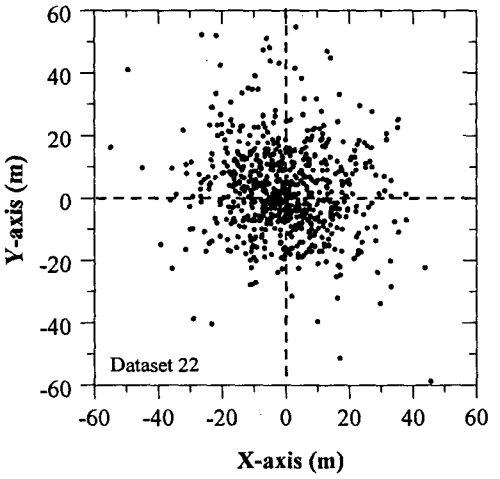

FIG. 4. Positions of detected breaking waves relative to the hydrophone array superimposed for a 30-min period (dataset 22).

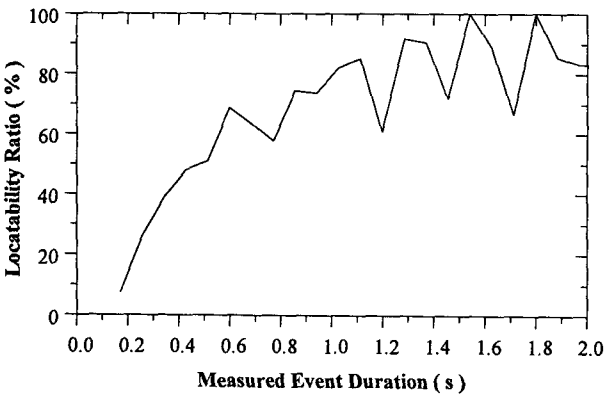

FIG. 5. Locatability ratio versus the measured duration D at the hydrophone array (dataset 3). The ratio increases from 10% to 70% as the duration D increases from 0.2 to 0.6 s. For $D > 0.6$ s, the ratio fluctuates between 60% and 100% with a mean value of 70%. These large fluctuations are possibly due to fewer events at greater duration.

shows the locatability ratio as a function of measured event duration (without the ML correction described in appendix B). The ratio increases rapidly from 10% to 70% as the duration D increases from 0.2 s to 0.6 s. The low locatability for $D < 0.6$ s can be explained as follows: the detected events below this scale contain a considerable amount of noise because of low source intensities so that the number of detected events is larger than it should be. The noise, however, is unlikely to appear simultaneously on two hydrophone pairs and is thus filtered out from located events determined using two hydrophone pairs. As a result, the locatability ratio is reduced. For $D > 0.6$ s, the ratio fluctuates between 60% and 100% with a mean value of 70%. These large fluctuations are due to fewer events at greater duration (the number in each bin is 50–60 for $D < 0.6$ s and 10–30 for $D > 0.6$ s) and do not show an intrinsic dependence on the duration.

For a uniform position distribution of events, $D = 0.6$ s corresponds to a mean duration of 1.15 s with the maximum likelihood correction. Above this scale, we do not expect the duration distribution to be severely affected by finite source dimension. Below this scale, the locatability ratio is contaminated by noise, which is difficult to evaluate. Nevertheless, our primary concern is the mean scale of breaking, which is better represented by event speed.

The effect of finite source dimension on the speed distribution can only be addressed indirectly, due to the inability to obtain the speed of nonlocatable events that can only be detected on one hydrophone pair. The only information about nonlocatable events available for such analysis is time delay of signals between hydrophones, and we can calculate the rate of change of the time delay for each source as it moves through the field of observation. This rate depends on the velocity and position of the breaking event. If it is assumed that the positions of breaking events are uniformly distributed, the probability distribution of the rate of change is determined by the event velocity. Therefore, we calculate the rate of change for nonlocatable events that can be detected on the hydrophone pair oriented in the wind direction. This pair usually has most of the nonlocatable events, since it is more nearly perpendicular to the wave crest and thus detects more coherent signals (Farmer and Ding 1992). The apparent speed distribution for the nonlocatable events (using dataset 3 in Table 1) is shown in Fig. 6a compared with the distribution for the trackable events in Fig. 6b. Although the details of these distributions differ, the dominant speeds are similar. Therefore, on the basis of this limited information, we conclude that the finite source dimension effect does not selectively eliminate breaking events at a particular speed and that the speed distribution is not significantly modified.

The dataset used in this example was acquired at a relatively steady and high sea state. Incomplete measurement is not expected to affect calculation of breaking wave distributions at scales greater than the scale described here.

4. Results

Our observations consist of 23 datasets during 4 deployments of the hydrophone array, over the period of

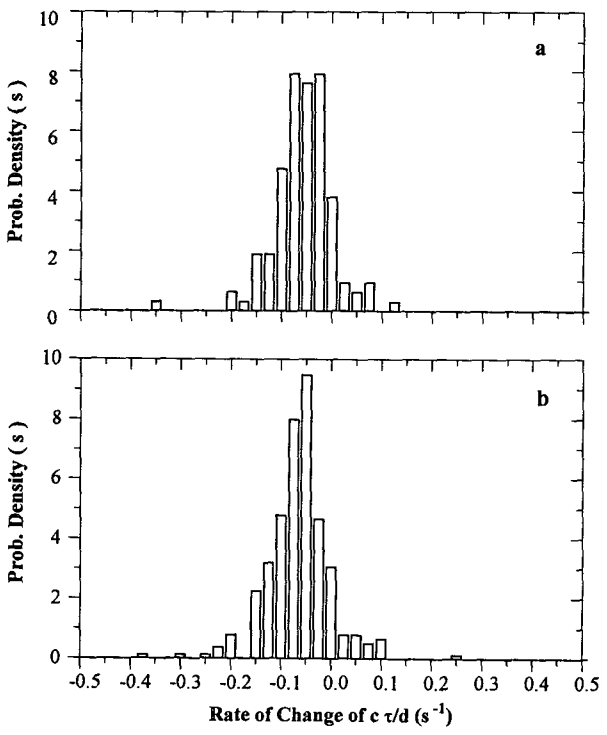

FIG. 6. Distribution of the rate of change of $c\tau/d$, where τ is the time delay of signals arriving at the hydrophone pair oriented in the wind direction, c is sound speed, and d is the spacing between the hydrophones. (a) For nonlocatable events; (b) for tracked events (dataset 3).

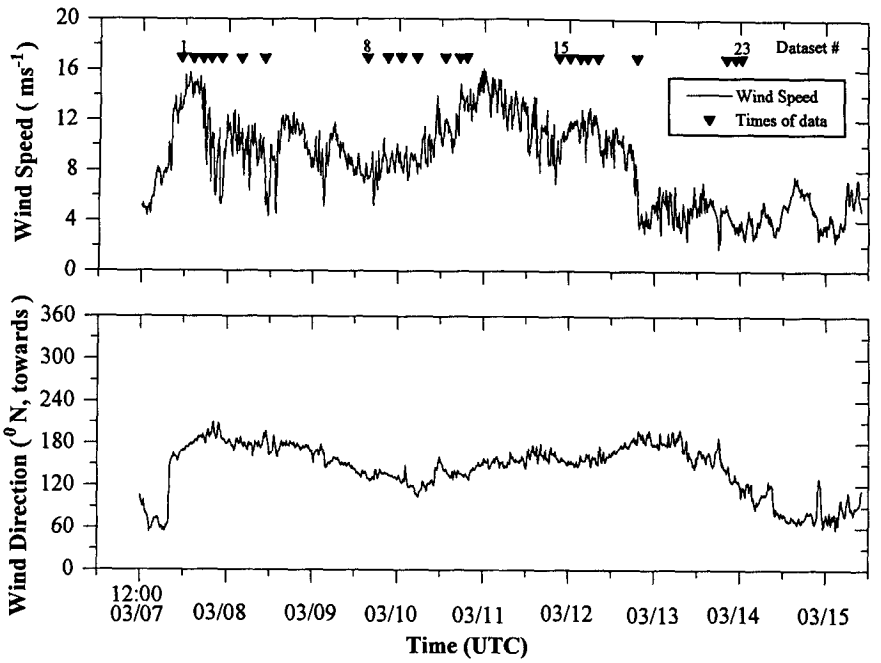

FIG. 7. Time history of the wind velocity during part of the SWAPP experiment. Raw wind data (provided by A. Plueddemann, WHOI) were measured at 22 m above the water. The periods during which the acoustical data presented in this paper were acquired are marked by solid downward triangles.

7–14 March 1990 (Fig. 7). Wind velocity was measured every minute by a Vector Averaging Wind Recorder (VAWR) on *FLIP*, at about 22 m above the water. Air and sea surface temperatures were also measured. Table 1 shows wind and wave conditions for each acoustic dataset we analyzed, where the wind speed was averaged over one hour enclosing the period of the dataset, and has been adjusted to a standard 10 m height using the air–sea temperatures listed in Table 1. The adjusted wind speeds are used in the subsequent analysis. For each acoustic dataset, breaking event statistics were obtained in an area of radius 30–40 m and over a period of 30 min (except datasets 15 and 19, which are 15 min), and the number of events in each dataset is normally between 350 and 700, depending on the sea state. The results are given in Table 2.

a. Definition of breaking wave properties

Our observations are used to derive statistical results for three different properties: breaking event density, duration, and velocity. Event density ($\hat{Q}$) is defined as the number of events per unit area per unit time. It can be determined by the number of detectable events in a selected observation area and the detection probability of events. The number of detectable events is obtained by dividing the number of locatable events by the locatability ratio. This ratio ranges from 65% at higher winds (14 m s^{-1}) up to 85% at lower winds (6 m s^{-1}). The detection probability depends on the required signal to noise ratio, which can be estimated from the data. The estimation of event density is discussed in appendix D.

Event duration is obtained by comparing the measured durations in the correlation images from all possible hydrophone pairs and choosing the longest; this value is corrected with the maximum likelihood estimator. Event velocity however is directly measured without necessity of correction and is relative to the instrument, which is considered stationary relative to the surface drifting layer since it drifted at approximately the same speed as the layer (Ding and Farmer 1992a). Downwind dimension L_D, defined as the distance a breaking event travels, is given by the product of event speed and duration; that is, $L_D = vD$. The duration distribution of locatable events and the velocity distribution of trackable events can also be obtained in the same observation area as above.

From these properties, we also evaluate the mean spacing between breaking waves. Consider an observation area S where there are N breaking events with mean spacing $\bar{l}_s$. Then $S \approx N\bar{l}_s^2$ *when* N is large and the area of breaking events is small compared to $\bar{l}_s^2$. Given breaking density $\hat{Q}$ as defined above, the number of events occurring in S and during the mean lifetime $\bar{D}$, is $N = \hat{Q}\bar{D}S$. Therefore, the mean spacing can be estimated by

TABLE 1. Wind and wave conditions for the SWAPP data. W_{10} and θ_w: wind speed at 10 m and wind direction; T_s and θ_s: period and direction of the swell; T_p and θ_p: period and direction of the peak wind wave; β: slope of the elevation spectrum; t_w: water temperature; t_a: air temperature. Starting times and dates of the datasets are also given in UTC. The directions are relative to truth north (toward).

Dataset	Date (mo/day)	Time (UTC)	W_{10} (m^{-1})	θ_w (deg)	T_s (s)	θ_s (deg)	T_p (s)	θ_p (deg)	β	t_w (°C)	t_a (°C)
1	03/07	2246	13.7	170	10.7	129	4.92	125	−5.89	13.02	11.38
2	03/08	0201	13.5	186	9.1	134	5.20	146	−6.00	12.94	10.27
3	03/08	0446	9.9	191	10.7	131	7.68	144	−5.21	12.94	9.48
4	03/08	0701	7.7	191	10.7	133	5.48	164	−5.78	12.93	9.48
5	03/08	1001	10.2	178	10.7	135	7.10	147	−5.75	12.85	9.67
6	03/08	1531	10.2	176	12.0	136	6.86	155	−5.56	12.80	9.33
7	03/08	2201	10.5	172	10.1	142	5.49	152	−5.21	12.84	9.79
8	03/10	0301	8.4	131	12.8	149	5.20	122	−5.05	12.83	13.13
9	03/10	0846	8.4	117	12.8	144	4.47	116	−5.02	12.80	13.13
10	03/10	1231	9.0	119	11.3	145	5.60	123	−4.76	12.95	13.07
11	03/10	1701	10.0	136	12.8	139	4.50	123	−5.67	13.10	12.98
12	03/11	0101	13.8	149	12.0	132	6.62	115	−5.17	13.87	11.92
13	03/11	0501	13.6	155	12.8	130	6.40	134	−5.63	13.87	10.96
14	03/11	0701	12.4	151	10.1	135	7.11	135	−5.37	13.80	10.17
15	03/12	0901	9.5	159	10.7	134	5.30	147	−5.54	13.18	10.65
16	03/12	1201	9.9	170	8.7	128	5.60	143	−5.54	13.17	11.03
17	03/12	1501	9.1	178	13.7	141	4.00	153	−5.57	12.88	11.03
18	03/12	1701	6.6	181	13.7	141	4.00	153	−5.57	12.87	11.16
19	03/12	2001	4.4	183	12.8	138	3.15	179	−6.34	12.92	11.00
20	03/13	0701	4.9	155	12.0	142	3.56	164	−5.60	12.77	10.83
21	03/14	0801	5.9	73	10.7	129	2.74	66	−6.43	12.80	12.20
22	03/14	1031	6.1	70	10.1	129	3.10	68	−6.75	12.75	12.38
23	03/14	1215	5.8	80	10.1	126	3.20	64	−6.34	12.75	12.70

$$\bar{l}_s \approx \frac{1}{\sqrt{\bar{Q}\bar{D}}}. \tag{2}$$

Note that this is an overall average and independent of direction.

It is also of interest to calculate a property that is an acoustic analog of whitecap coverage. We define "active acoustic coverage" as the fraction of the sea surface swept by active acoustic events during their lifetime. The mean area swept by each individual event is given by $\epsilon = \overline{L_D L_c}$, where L_c is the cross dimension. Bortkovskii's data (1987), obtained photographically, show that the correlation coefficient between the downwind dimension and crosswind dimension of whitecaps varies from 0.15 to 0.78 in the Southern Ocean and from 0.28 to 0.85 in the tropics, but that this correlation is rather scattered, showing no clear dependence on the wind speed and the whitecap size. Due to scarce information about the correlation, we assume for this calculation that the crosswind dimension is independent of the downwind dimension; better estimation of ϵ could be achieved with further development of the measurement technique. The mean crosswind dimension of a breaking wave is estimated by Bortkovskii to be twice the mean downwind dimension; that is, $\epsilon = 2\bar{L}_D^2$. Then acoustic coverage as a fraction of the sea surface is given by

$$\mathrm{AC} = \frac{N\epsilon}{S} = \frac{\epsilon}{\bar{l}_s^2} = \frac{2\bar{L}_D^2}{\bar{l}_s^2}. \tag{3}$$

b. Wave spectra

Directional wave spectra measured with Doppler sonars are limited to waves of period longer than 2 s ($\lambda = 6.42$ m). These data are in the form of the velocity spectrum $V(\omega, \theta)$, but can be transformed to the elevation spectrum or acceleration spectrum by multiplying $V(\omega, \theta)$ by ω^{-2} or ω^2. The frequency spectrum can be obtained by integrating the directional spectrum with respect to the angle:

$$V(\omega) = \int_0^{2\pi} V(\omega, \theta) d\theta.$$

For a directional spectrum, the direction of waves at frequency ω is defined as

$$\theta(\omega) = \tan^{-1} \frac{a(\omega)}{b(\omega)}, \tag{4}$$

where

$$a(\omega) = \int_0^{2\pi} V(\omega, \theta) \sin\theta d\theta,$$

$$b(\omega) = \int_0^{2\pi} V(\omega, \theta) \cos\theta d\theta,$$

and θ is with respect to true north. Figure 8a shows an example of the velocity spectrum at a 9.9 m s^{-1} wind speed (dataset 3 in Table 1), in which there is a swell component at 11 s. [These sonar spectra were derived

using a more complicated approach than the standard Fourier transform method, and calculated confidence intervals are not yet available (J. Smith 1993, personal communication).] For all the available spectra, the swell has a period of 10–13 s for θ between 120° and 150°. A second peak at 7.68 s in Fig. 8a can also be identified, which is believed to correspond to the dominant wind wave component. The velocity spectrum is shown here since the Doppler sonar directly measures particle velocity. Transformation of the velocity spectrum to the elevation spectrum, which is more typically used in wave studies, renders the second peak less readily distinguishable in this example. At higher winds, separation of the dominant wind wave peak is not always obvious. In these cases, we use the wind history as an additional reference: if the wind has been blowing steadily for more than 6–8 hours, then the sea state is considered steady, and we choose the dominant peak whose corresponding phase speed does not exceed the wind speed.

Spectra at lower winds show better defined dominant wind wave peaks, for example, in Fig. 8b for dataset 22 (datasets 21 and 23 also have a clear wind wave peak). The peak period in this case is 3.1 s. The peak period (T_p) and direction (θ_p) for each dataset are listed in Table 1. In general, the velocity spectral peak differs by less than 8% from the elevation spectral peak if both are identifiable.

We can also determine the slope of the spectrum for wind waves, s, defined by

$$V(\omega) \sim \omega^s.$$

The slope was calculated by linear regression using the logarithm of the spectrum in the wind wave region between the second peak and the high-frequency cutoff. The slope of the elevation spectrum is then given by $\beta = -2 + s$. The elevation spectral slope is also included in the table for reference.

c. *Breaking event density*

Previous results on breaking wave properties such as whitecap coverage are generally expressed in the form of a power law. In the following presentations of our results, we use a log–log display in order to facilitate comparison. Figure 9a shows breaking event density as a function of wind speed from the SWAPP data (solid circles). The event density lies in the range of 0.2–1.1 ($\times 10^{-3}$ m^{-2} s^{-1}) for these data. It is interesting to see that, although scattered, the density actually decreases with increasing wind. A likely explanation would be that the dominant breaking wave scale increases with increasing wind, resulting in a decrease in the total number of breaking waves detected per unit observation area. Note that due to background noise, the instrument can only detect discrete and relatively loud noise sources, which are believed to be associated with dominant breaking waves. Therefore, this explanation only applies to larger breaking waves. As pointed out by one of our reviewers, small breakers that might be detected at lower winds may not rise above back-

TABLE 2. Breaking wave statistics from the *SWAPP* data. $\hat{Q}$: event density; $\bar{D}_e$: event duration; $\bar{V}_e$: event speed; $\bar{\theta}_e$: event direction of motion; $\bar{L}_D$: downwind dimension; $\bar{c}_{br}$: mean breaking wave speed; $\bar{\theta}_{br}$: mean breaking wave direction; m_4: the fourth moment of the spectrum. The directions are relative to true north (toward).

Dataset	$\hat{Q}$ ($\times 10^{-3}$) (m^{-2} s^{-1})	$\bar{D}_e$ (s)	$\bar{V}_e$ (m s^{-1})	$\bar{\theta}_e$ (deg)	$\bar{L}_D$ (m)	$\bar{c}_{br}$ (m s^{-1})	$\bar{\theta}_{br}$ (deg)	m_4 (m s^{-2})^2
1	0.551	1.71	4.67	162	9.61	5.38	136	0.501
2	0.311	1.71	5.48	181	11.49	6.99	152	0.699
3	0.246	1.69	5.39	170	11.41	6.55	163	0.606
4	0.422	1.64	4.98	192	10.63	6.22	172	0.572
5	0.378	1.55	5.06	183	10.67	5.84	170	0.539
6	0.426	1.41	4.65	183	8.31	5.56	174	0.445
7	0.429	1.70	4.63	176	9.79	4.72	171	0.311
8	0.643	1.51	3.81	125	7.36	4.37	116	0.295
9	0.553	1.40	4.25	92	8.09	4.80	105	0.391
10	0.516	1.44	4.43	107	8.32	4.49	102	0.313
11	0.382	1.56	4.59	134	8.30	4.93	123	0.424
12	0.289	1.78	5.46	137	11.54	5.97	127	0.569
13	0.303	1.61	5.39	150	11.17	6.26	139	0.630
14	0.337	1.79	5.31	144	12.00	6.39	137	0.635
15	0.818	1.49	4.58	160	8.83	5.31	149	0.447
16	0.381	1.44	4.46	157	7.87	5.19	150	0.432
17	0.678	1.37	4.40	177	7.57	5.30	162	0.397
18	0.529	1.40	3.88	182	6.53	5.30	162	0.397
19	0.656	1.42	3.74	181	6.17	5.86	168	0.410
20	0.720	1.18	3.34	167	4.68	4.75	168	0.233
21	1.063	1.29	3.18	61	4.44	3.75	62	0.186
22	0.770	1.40	3.30	55	5.54	3.90	58	0.231
23	0.688	1.30	3.32	64	5.10	4.08	61	0.245

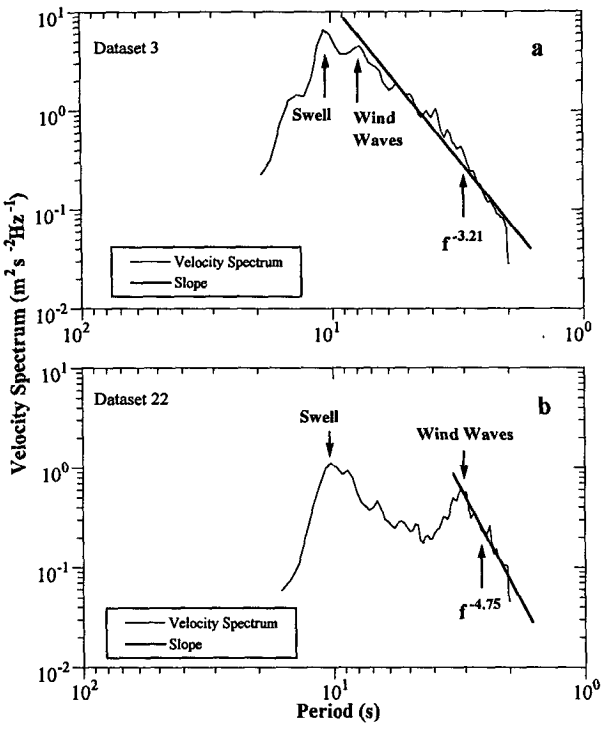

FIG. 8. Velocity spectrum measured by the Doppler sonar on RP *FLIP* for (a) dataset 3 and (b) dataset 22 in the table. The arrows show the swell and the peak wind wave component. The solid curve indicates the slope of the spectrum in the wind wave region.

ground noise (which increases with wind speed) or may become too numerous to be detected at higher winds. Smaller breakers and particularly microbreakers may occur so often that they blend together into continuous sources at strong winds and may also be modulated by underlying longer waves as suggested by Zedel and Farmer (1994).

Snyder et al. (1983) measured breaking wave density with a camera over the wind speed range 2–8 m s^{-1}. We plot their results (stars) together with our results for comparison. It can be seen that their data are considerably more scattered, especially at winds between 6 and 7 m s^{-1}, possibly because they were collected in a fetch-limited sea where waves were still developing or there were fewer events collected for statistical analysis. Nevertheless, there is overlap between these two datasets at winds between 4 and 7 m s^{-1}, although they were acquired with different techniques. The event density is also plotted in Fig. 9b against the inverse wave age, W_{10}/C_p, where W_{10} is the wind speed at 10 m and C_p the dominant wave phase speed obtained from T_p in Table 1. Our data show no significant dependence on the wave age, possibly because the sea states were essentially fully developed. The data of Snyder et al. have a tendency toward increased density with inverse wave age apparently due to the fact that their data were acquired in a fetch-limited sea.

d. Event velocity and duration

Figures 10a–c show the speed distribution of trackable events at wind speeds of 6.1, 10.0, and 12.4 m s^{-1} (datasets 22, 11, 14), where the arrow indicates the mean speed, which increases with the wind but is substantially less than the wind speed. It can be seen that the distribution is narrower at lower wind speeds, and spreads as the wind increases. As discussed in section 3c, the incomplete measurement of the instrument has no significant effect on the speed distribution at scales above 1.8 m s^{-1} for high sea states (Fig. 10c). For a lower sea state as in Figs. 10a (dataset 22), this scale decreases to 1.1 m s^{-1}.

Figures 11a–c show the corresponding distributions of event direction of motion, which are seen to be generally aligned with the wind direction. The mean event direction is defined as

$$\bar{\theta}_e = \tan^{-1} \frac{\bar{v}_y}{\bar{v}_x}, \tag{5}$$

where $\bar{v}_y$ and $\bar{v}_x$ are the mean x and y components of the event velocity. This value is 55°, 134°, and 144° for these examples, compared to their corresponding wind directions, which are 70°, 136°, and 151°, respectively.

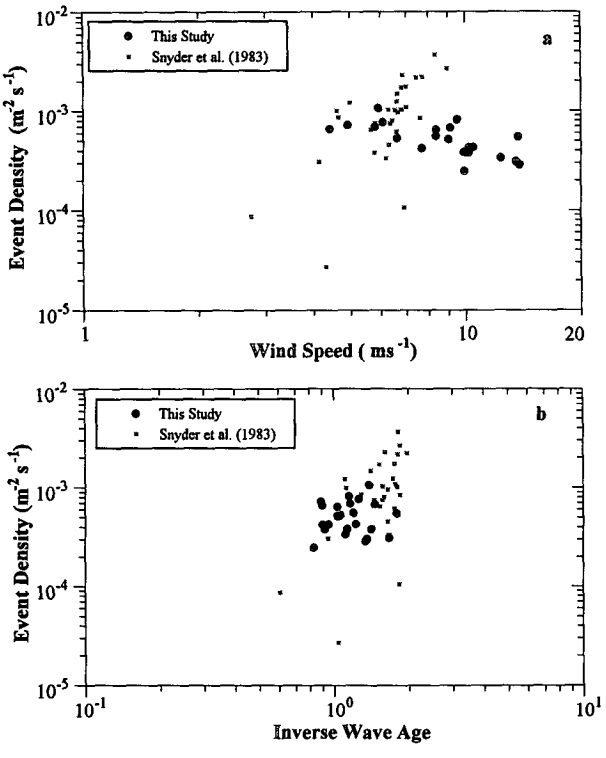

FIG. 9. Breaking event density versus (a) wind speed at 10 m, and (b) inverse wave age. The solid circles represent the SWAPP data and the stars are from the data of Snyder et al. These data are plotted on a log–log scale.

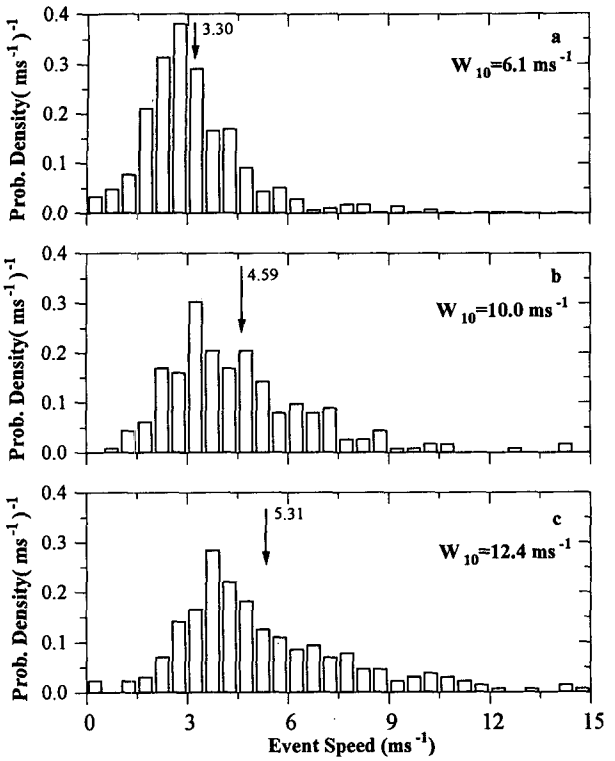

FIG. 10. Event speed distribution at three wind speeds at 10 m. The arrow indicates the mean event speed. (a) W_{10} = 6.1 m s^{-1}, (b) W_{10} = 10.0 m s^{-1}, and (c) W_{10} = 12.4 m s^{-1}, corresponding to datasets 22, 11, 14 in the table.

Figures 12a–c show the duration distribution of locatable events for the same data as above. Comparing with Fig. 10, we can see that the duration distribution is more asymmetric, showing higher densities on the left and a longer tail on the right. Similar to Fig. 10, the duration distribution is broader as the wind increases. In section 3c, it is estimated that the duration is not severely affected by incomplete measurement for scales above 1.15 s.

Figure 13a shows mean event speed against wind speed. The mean event speed is approximately 0.7 of the wind speed at 5.0 m s^{-1} and drops to 0.4 at 14.0 m s^{-1}. (There will be more discussion on this issue in section 5.) Since small events may be lost due to background noise, the mean event speed (and also duration and downwind dimension below) is expected to be larger than the true value. This problem is addressed in appendix C.

In Fig. 13b, we show the dependence of mean duration on wind speed. The mean duration ranges from 1.2 s at 5.0 m s^{-1} to 1.7 s at 14 m s^{-1}, and increases with the wind speed. Snyder et al. (1983) observed that the duration of whitecaps was of order 0.5 s for wind speeds from 2 to 8 m s^{-1}. Wu (1992) has suggested that this lack of wind dependence may arise because their measurements were made in a fetch-limited sea; normalization of their data by the dominant wave period shows a dependence on the wave period.

e. Downwind dimension

Figure 13c shows the dependence of mean downwind dimension on wind speed. Although there is considerable scatter, these data can be fitted using linear regression to a power of 0.79 dependence (the resulting power has a deviation of 0.1). Previous observations of the downwind and crosswind dimensions of whitecaps in the Southern Ocean and tropical ocean are given in Bortkovskii (1987). Although the data are scattered, the characteristic length, defined as $s = \sqrt{\bar{L}_D \bar{L}_c}$, appears to be well approximated by a power of 0.75 dependence on the wind speed (Wu 1992), which is comparable to our present result in Fig. 13c. However, the downwind dimension determined from our data is considerably larger (2–4 times) than that given by Bortkovskii. This is discussed in section 5b.

f. Mean spacing and active acoustic coverage

The dependence of mean spacing and of active acoustic coverage on wind speed are shown in Figs. 13d and 14, respectively. The mean spacing has an increasing trend as the wind increases, varying from

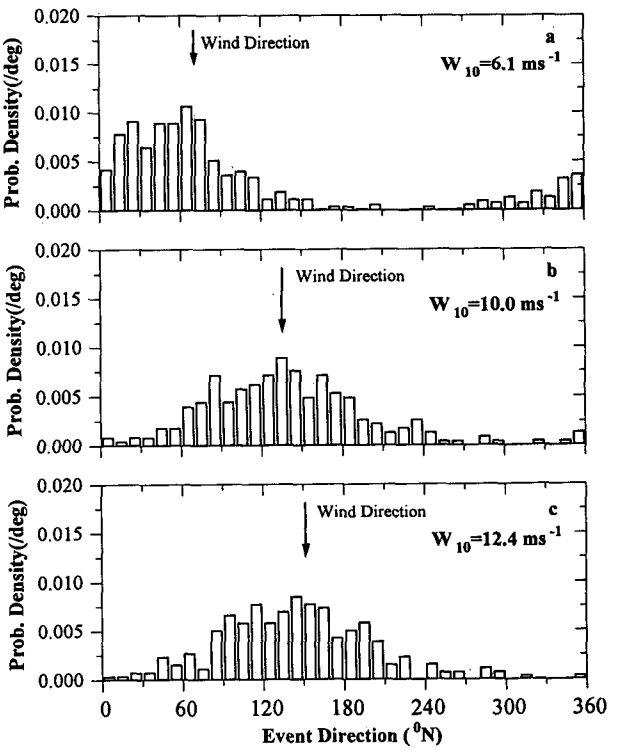

FIG. 11. Event direction distribution for the same data as in Fig. 10. The wind direction indicated by the arrow is toward (a) 70°, (b) 136°, and (c) 151°, (true north).

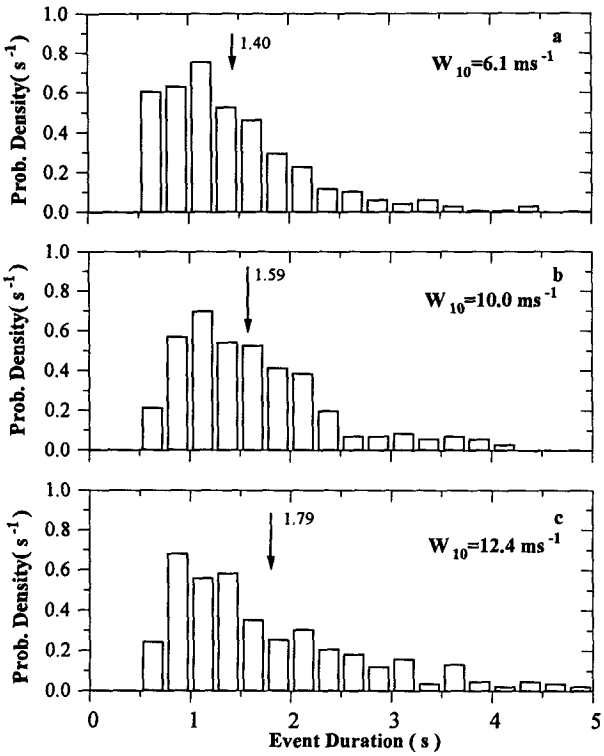

FIG. 12. Event duration distribution for the same data as in Fig. 10. The arrow indicates the mean duration.

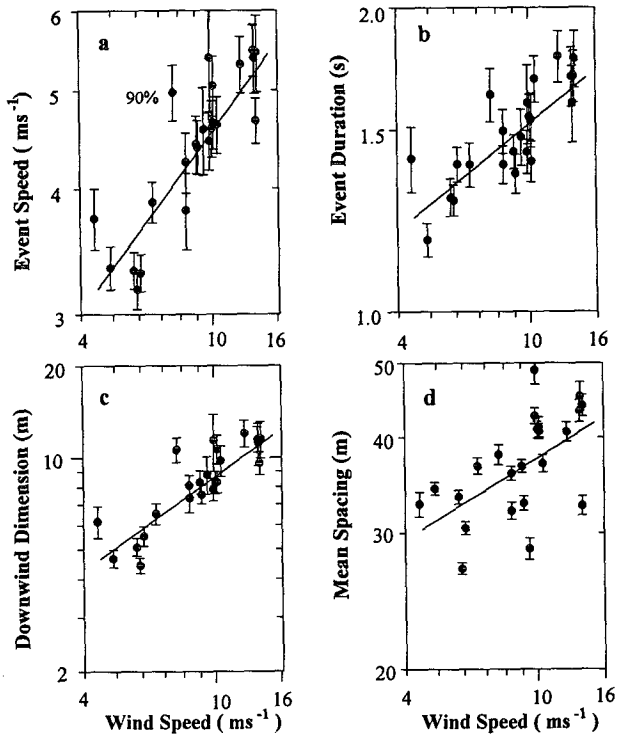

FIG. 13. Event statistics versus wind speed at 10 m. Data are plotted on a log–log scale. The straight lines are the linear regression of the data. (a) Mean event speed, slope = 0.45; (b) mean duration, slope = 0.27; (c) mean downwind length, slope = 0.79; and (d) mean spacing, slope = 0.27. A 90% confidence interval is also shown for each data point.

about 30 m at a wind speed of 4 m s^{-1} to about 45 m at 14 m s^{-1}. The active acoustic coverage, varying from 4% to 14% for the same wind speeds, shows a nearly linear dependence on the wind speed (a power of 1.03 with a 0.19 deviation). This is unlike the 3.75 power relation between whitecap coverage and wind previously obtained by Wu (1979), but consistent with the observations of active whitecap coverage by Bortkovskii (1987), who distinguished between the active breaking crest of waves and the foam produced by the breaking crest. The explanation is that previous whitecap observations usually include both active whitecaps and foam, thus resulting in a much more rapid increase with wind. Our acoustic observation is derived from the sound radiated primarily by active breaking crests where bubbles are injected, and is therefore more consistent with Bortkovskii's measurements of active whitecap coverage. Note that our acoustic coverage is significantly larger than his whitecap coverage (below 5% for the same wind speeds), apparently due to the different observation techniques, as discussed in section 5b. Nevertheless, the absolute magnitude is not what we are seeking here. It is the dependence on the wind speed that is of interest.

Wu (1992) derived a wind dependence of mean spacing between whitecaps, which is nearly inverse

$$\bar{l}_s \sim U_{10}^{-1.07},$$

instead of an increasing dependence as in our data. The power dependence of whitecap dimension on wind used by Wu was 0.8, close to that in Fig. 13c. Thus, the difference in the wind dependence of mean spacing is clearly caused by the use of the higher power (3.75) dependence of whitecap coverage on wind.

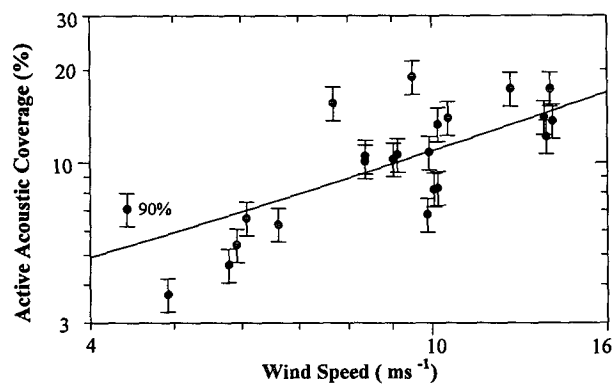

FIG. 14. Dependence of active acoustic coverage on wind speed at 10 m. Data are plotted on a log–log scale. The straight line is the linear regression of the data; slope = 1.03. A 90% confidence interval is also shown for each data point.

5. Discussion

a. The scale of breaking

To describe the characteristics of wave breaking, it is useful to have some measure of the breaking scale. Phillips (1985) suggested the use of the velocity of breaking waves as a measure of the breaking scale since it is a well-defined parameter; it is often difficult to define an unambiguous parameter from the local surface configuration at one given instant or from the time history at one given location. Our observations provide direct measurement of this velocity, which will therefore be used as a measure of the kinematic scale of breaking in the subsequent discussion.

It has been observed in the preceding section that the measured speed of breaking events is 0.4–0.7 of the wind speed. In a fully developed sea where the dominant wave phase speed C_p is close to the wind speed, this result implies that the mean breaking event speed is considerably smaller than C_p. In the absence of underlying longer waves, bubbles injected by breaking waves are advected at the particle velocity near the crest, which is close to the phase velocity. This has been observed in a fetch-limited sea by detecting bubbles generated by wave breaking with active sonar (Thorpe and Hall 1983). Since sound is believed to be generated by bubble formation, acoustic sources associated with breaking waves at some frequency should travel at a speed close to the phase speed, at least at the stage of active breaking. The fact that the mean event speed in a broadband wave field is considerably smaller than C_p implies the importance of higher-frequency components, since breaking waves with higher frequencies travel at smaller speeds than the dominant wave.

Let us assume that the travel velocity of breaking waves at some frequency is equal to the corresponding phase velocity. It is desirable to derive from the wave spectrum some mean velocity comparable to the mean event velocity. The probability of wave breaking [see Eq. (9) below] derived by Snyder and Kennedy (1983) depends on the fourth spectral moment, which is physically the variance of downward acceleration. Therefore, it is not unreasonable at this stage to weight the contribution from each component with the acceleration spectrum to derive the mean velocity; this yields reasonable results as seen below, although further theoretical work is needed to develop a more realistic approach.

In the linear approximation, the Lagrangian and Eulerian accelerations are equivalent. We can therefore derive the acceleration spectrum from the velocity spectrum using

$$A(\omega, \theta) = \omega^2 V(\omega, \theta).$$

The mean speed of breaking waves is defined as

$$\bar{c}_{br} = \frac{1}{m_4} \int_{\omega_1}^{\omega_2} c(\omega) A(\omega) d\omega, \tag{6}$$

where

$$A(\omega) = \int_0^{2\pi} A(\omega, \theta) d\theta$$

and

$$m_4 = \int_{\omega_1}^{\omega_2} A(\omega) d\omega \tag{7}$$

is the fourth moment of the elevation spectrum or the variance of vertical acceleration between ω_1 and ω_2, and $c(\omega)$ is the phase speed at frequency ω. The mean direction of motion is defined as

$$\bar{\theta}_{br} = \tan^{-1} \frac{a}{b}, \tag{8}$$

where

$$a = \int_{\omega_1}^{\omega_2} c(\omega) \int_0^{2\pi} A(\omega, \theta) \sin\theta d\theta d\omega$$

$$b = \int_{\omega_1}^{\omega_2} c(\omega) \int_0^{2\pi} A(\omega, \theta) \cos\theta d\theta d\omega.$$

Each of the parameters m_4, $\bar{c}_{br}$, and $\bar{\theta}_{br}$, is obtained by integrating the acceleration spectrum from the dominant peak to the high-frequency cutoff. The results are included in Table 2 for comparison. It can be seen that $\bar{V}_e$ is close to, but slightly smaller than, $\bar{c}_{br}$ (75%–95% of $\bar{c}_{br}$).[2] The difference can be explained in part by the fact that our instrument is able to measure breaking events with speeds down to 1.5 m s^{-1} (Fig. 10), much smaller than the high-frequency cutoff of the Doppler sonar (0.5 Hz corresponds to a phase speed of 3.12 m s^{-1}).

We therefore conclude that the observed mean event speed is an average result of the contributions from different wave components in the spectrum. It is of interest to compare the mean breaking scale ($\bar{V}_e$) with the dominant wave scale (C_p). Figure 15a shows the mean event speed normalized by C_p (obtained from

[2] Long-wave advection should be examined here. As mentioned earlier, the measured velocity is relative to the instrument, which is stationary relative to the mixed layer. In the presence of underlying swell, $\bar{c}_{br}$ is the phase speed in the moving medium, which in this case is the current induced by the swell. Swell typically has a period of 10–13 s for the datasets (Table 1), and the amplitude is estimated from the pressure sensor and accelerometer on the instrument to be of order of 1.35 m. Taking a swell period of 10 s, which gives the largest correction, yields a particle velocity $u_0 = 0.85$ m s^{-1}. Consider dataset 21 in Table 1, for which the mean event speed is the smallest (3.18 m s^{-1}) and the angle between the event velocity and swell is 68°. The event speed relative to the moving medium is therefore

$$V'_e = V_e - u_0 \cos\theta = 2.85 \text{ m s}^{-1}$$

at most, some 10% smaller than the absolute speed. Note that the instrument is also moved by the orbital velocity of the swell, but the motion is in phase with the advection at the surface. The above estimate therefore represents an upper bound on the error.

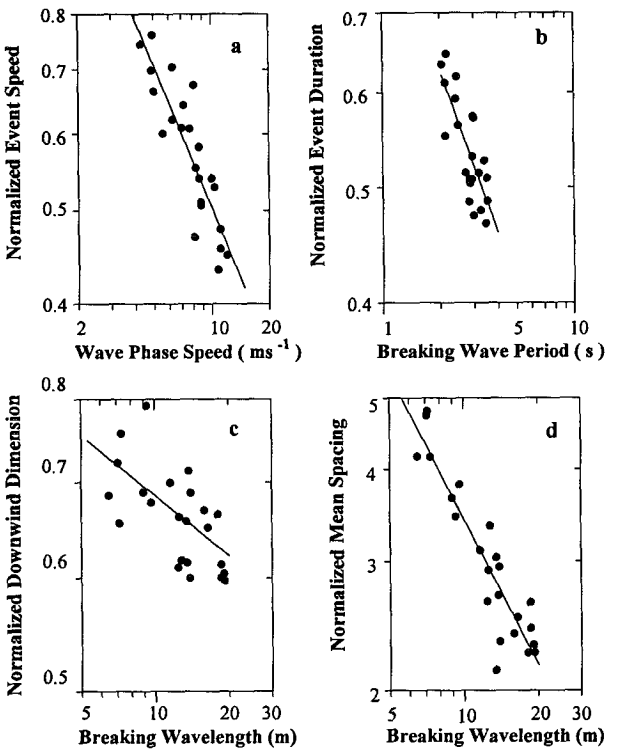

FIG. 15. Normalized event statistics. The normalization is with respect to the corresponding abcissa variable. Data are plotted on the log–log scale. The straight lines are the linear regression of the data. (a) Normalized event speed, slope = −0.49. (b) Normalized breaking duration, slope = 0.45. (c) Normalized downwind length, slope = −0.14. (d) Normalized mean spacing, slope = −0.66.

T_p in Table 1). It is seen that $\bar{V}_e$ is about 75% of C_p at lower C_p (4 m s^{-1}) and decreases down to 45% as C_p increases to 12 m s^{-1}. This decreasing trend can be explained as follows: since the instrumental cutoff for measurement of event speeds is fixed (of order 1.5 m s^{-1}), as the dominant wave phase speed C_p decreases, the frequency range over which the wave components are averaged [as in Eq. (6)] becomes smaller, and thus the resulting mean event speed is closer to C_p.

Two recent studies have examined possible scales of breaking waves that supply wave energy to the mixed layer. Thorpe (1993) used laboratory measurements of wave energy dissipation rate in quasi-steady breaking waves and field observations of wave breaking frequency to estimate total energy loss due to breaking, and found that if the dissipated energy were to support the turbulent energy in the mixed layer, the breaking scale (phase speed) would be 25% of the dominant scale. Melville (1993), however, found this ratio would be 63% if laboratory measurements of dissipation rate in spilling unsteady breaking waves (which is lower than in quasi-steady waves for the same scale) were used (he also assumed a thinner surface layer with a higher dissipation rate). While microbreakers may be quasi-steady, unsteady breaking waves seem more realistic in the open ocean, especially for larger-scale breaking waves. Melville's argument for unsteady waves appears to be consistent with our observations, which show the ratio is 45%–75%. Thorpe's estimate would probably be important for small-scale breakers, which are difficult to detect with our present approach.

b. *Normalization by the breaking scale*

As discussed above, the mean kinematic scale ($\bar{V}_e$) may be equated to wave phase speed, which can be used to infer the corresponding time scale (period $\bar{T}_{br}$) and length scale (wavelength $\bar{\lambda}_{br}$) via the dispersion relation for surface gravity waves. We may then use these scales to normalize the observed breaking wave statistics.

Figure 15b shows the ratio of the mean breaking duration to the mean breaking period $\bar{T}_{br}$. The mean duration is 45%–65% of $\bar{T}_{br}$. Wu (1992) normalized the results of Snyder et al. on the whitecap duration by the dominant wave period, resulting in a ratio generally below 25%, which is much smaller than our data. Thorpe and Hall (1983) found that individual breaking waves that vigorously entrain bubbles at their crest last for 30%–50% of the wave period. Since the sound from breaking waves is generated mainly by the entrained bubbles, Thorpe and Hall's results are closer to our results than to the results of Snyder et al. As mentioned in the preceding section, the downwind length and coverage of whitecaps observed from aircraft or shipboard are significantly smaller than our acoustical observations. We attribute the difference between the acoustical and optical results to the different measurement techniques; it is possible that the weaker stage of air entrainment that cannot be observed at a distance with photographic techniques is nevertheless acoustically detected with hydrophones. Updegraff and Anderson (1991) used a video camera and a hydrophone array placed very close to the sea surface (1 m) to observe microbreakers, and found that the microbreakers, although difficult to see at a greater distance, can actually generate detectable sound even at very low wind speeds. Since acoustical radiation is intrinsic to the breaking process, we consider it a more reliable signal of wave breaking than the visible manifestations such as whitecaps identified in photographic observations.

Figures 15c–d show downwind dimension and spacing normalized by the mean wavelength ($\bar{\lambda}_{br}$). The normalized downwind dimension is more scattered than the normalized duration, varying between 60% and 75% of $\bar{\lambda}_{br}$. The mean spacing is seen to drop from 5 to 2 times $\bar{\lambda}_{br}$ as the wavelength increases from 10 m to 25 m. The decrease of normalized spacing with increasing wavelength would imply an increase of the breaking probability with the breaking scale.

c. *Direction of motion of breaking events*

The event direction of motion ($\bar{\theta}_e$) in Table 2 is scattered in relation to the mean breaking wave direction

($\bar{\theta}_{br}$) and wind direction (θ_w). There are in general, however, three cases in which these three directions are related, as sketched in Fig. 16. The first is where these three directions are close (within ±10°; Fig. 16a). The small difference in the wave and event directions is likely due to the fact that the sonar cutoff is not high enough to include the smallest waves observed by the hydrophone array. In the second case, the wave and event directions are close but the wind direction is significantly different (e.g., dataset 3; see Fig. 16b). This behavior may be caused by the delay of waves in response to a change in wind direction. There is, however, a third case in which although the wave direction falls behind the wind direction, the event direction appears to follow the wind direction (e.g., datasets 1, 2, 4, 17, 19; see Fig. 16c). This phenomenon implies that wind action may affect the direction of motion of breaking events but this effect depends also on the history of wind and waves. A better understanding of this phenomenon would require a careful examination of the time history of wind, surface waves, and breaking event statistics, which is beyond the scope of this paper. For all these datasets, swell is seen to have no clear impact on the event direction, since, as we discuss above, the breaking scale is not small enough that advection by swell has a significant effect.

The direction of events at different scales provides more details of the directivity of breaking waves. Figure 17 shows the mean direction of breaking events as a function of event speed for dataset 1, together with the corresponding wave direction as a function of phase speed, as given in Eq. (4). The horizontal line is the wind direction. The event direction for speeds between 3–6 m s^{-1} is seen to follow the dependence of the wave direction on phase speed, but has an offset from the wave direction possibly due to the effect of wind action. The event direction at high speeds appears more uncertain, because the number of events is smaller resulting in more statistical fluctuations.

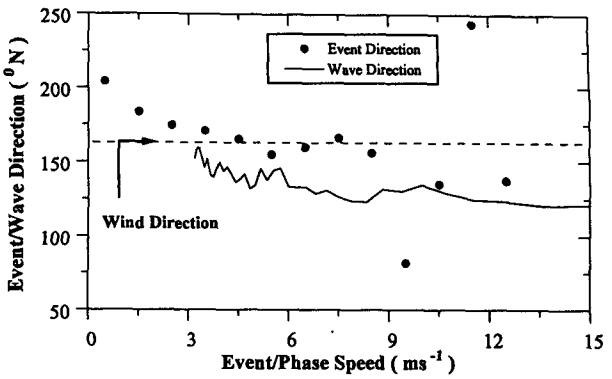

FIG. 17. Mean direction of motion for events against the event speed. The solid line is the wave direction as a function of phase speed, calculated using Eq. (4) and plotted in the same scale as the event speed for comparison. The horizontal dashed line is the wind direction.

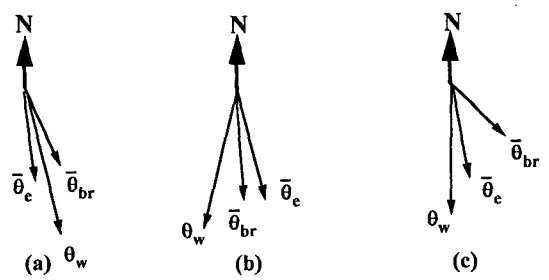

FIG. 16. Examples of the relationship between the mean direction of motion of events, the wave direction and the wind direction in three cases: (a) the three directions are basically aligned (dataset 7); (b) the wave and breaking event directions are close, but the wind direction is different (dataset 3); and (c) the event direction and wind direction are close but the wave direction is different (dataset 1). θ_w: wind direction. $\bar{\theta}_e$: breaking event direction as defined in Eq. (5). $\bar{\theta}_{br}$: wave direction as defined in Eq. (8); angles relative to true north.

d. *Breaking probability*

Previous theoretical and statistical studies of wave breaking have focused on the probability of breaking given a certain breaking criterion, either the steepness criterion (Ochi and Tsai 1983) or the acceleration criterion (Snyder and Kennedy 1983). Laboratory experiments (Ochi and Tsai 1983; Hwang et al. 1989) have also been carried out to test these theoretical models. It was found that by choosing an appropriate breaking threshold, the models generally agree with the experiments.

The Snyder and Kennedy model gives an expression for the breaking probability at any point on the surface:

$$P_{br} = 1 - \frac{1}{2}\,\mathrm{erf}\left(\frac{\alpha g}{\sqrt{2m_4}}\right), \qquad (9)$$

where m_4 is the fourth moment of the spectrum, and erf(x) is the error function. The breaking threshold α is defined such that a point is considered to break when its downward acceleration exceeds αg, with g being the gravitational acceleration. This probability is equivalent to the fraction of the sea surface covered by breaking water. Figure 18 shows the active acoustic coverage (from Fig. 14) as a function of m_4^{-1}, where m_4 is calculated from the directional wave spectra using Eq. (7). Equation (9) is fitted by least squares to these data to choose α, which was found to be 0.082. This value is extremely low compared with the one found in the laboratory by Ochi and Tsai (0.40) and that found by Snyder et al. (1983) in a fetch-limited sea (0.25–0.4). The low value of α partly reflects the sensitivity of the acoustic system to detection of breaking processes that do not show up for the same duration, or as often, as in other types of data. An additional factor is that m_4

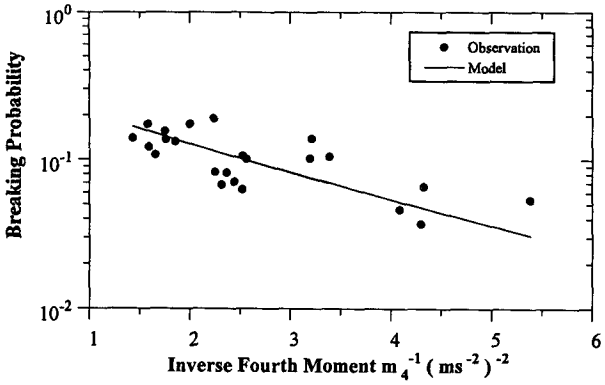

FIG. 18. Breaking probability measured as active acoustic coverage (as in Fig. 14) versus the inverse fourth moment determined from the sonar spectra. The solid line is the breaking probability predicted by the Snyder and Kennedy model (1983), given the same fourth moment and $\alpha = 0.082$. This α value is obtained by least-squares fitting of the model to the data.

is underestimated. As mentioned earlier, our instrument observes event speeds down to 1.5 m s^{-1}, corresponding to a frequency of 1 Hz, while the directional spectra provided by J. Smith from sonar measurements aboard *FLIP* have a cutoff at 0.5 Hz. Capacitance wire gauge spectra measured simultaneously with the sonar spectra show somewhat higher spectrum levels than the sonar spectra at higher frequencies, possibly implying that the sonar is less sensitive to higher-frequency components (J. Smith 1992, personal communication). Since m_4 is very sensitive to higher-frequency energy and depends crucially on the high-frequency cutoff, the real m_4 values for waves with scales down to 1 Hz can be appreciably larger than those estimated from the sonar spectra. Therefore, the α value determined from the sonar spectra is further underestimated.

With the chosen α and estimated m_4^{-1}, the predicted probability can be found from Eq. (9), which is also shown in Fig. 18 as the solid line. It can be seen that the observed probability generally agrees well with the predicted probability, with the standard deviation of the data from the curve being 0.007, which is small compared to the observed probabilities.

6. Summary

Our acoustical observation has for the first time provided comprehensive measurements of the spatial and temporal statistics of breaking surface waves in the open ocean. Despite limitations of the instrument, it has been possible to obtain the empirical dependence of breaking wave statistics on wind conditions. Comparison between the statistics and the simultaneously measured directional wave spectra has also led us to the following observations:

1) The observed distributions of breaking event speed cover a wide range from 1 to 10 m s^{-1}, indicating that wave breaking in the open ocean occurs at multiple scales. The mean breaking event speed is found to be considerably (45%–75%) smaller than the phase speed of the dominant wind wave, which we attribute to contributions from breaking waves with scales smaller than the dominant scale.

2) The directions of wind, waves, and breaking events are generally aligned. However, when the wind direction is significantly different from the wave direction, there is some evidence that the event direction lies closer to the wind direction, depending on the history of wind and waves.

3) It was found that the breaking threshold α determined from our field data using the Snyder and Kennedy model and the directional wave spectra is appreciably smaller than found by other investigators. This is partly attributed to the increased sensitivity of the acoustic method and partly to an underestimate of m_4 using the sonar data. Incomplete measurement of m_4, in which contributions from higher-frequency components are ignored, is an inevitable consequence of using a high-frequency cutoff determined by the available directional wave spectra, and has no intrinsic significance. More significant is the predicted dependence of the breaking probability on m_4 using the Snyder and Kennedy model, which appears to agree closely with our observations. It should be emphasized that the effects of the nonlinearity of wave breaking have not been considered in the present model. We speculate that the nonlinearity would affect the choice of α in the breaking criterion.

The wind dependence of breaking wave properties (Fig. 13) is generally quite scattered. Normalization by the breaking scale yields only a moderate reduction in scatter (Figs. 15a and 15d). The implication is that the observed breaking wave properties depend on more than just one or two parameters. We anticipate that greater insight may be derived by exploiting the detailed wave field information, using models that incorporate the intrinsic nonlinearity of the wave field.

It should also be emphasized that these results only apply to wave breaking at larger scales. Smaller breakers are more difficult to detect due to background noise and therefore part of them have been lost. An individual large-scale breaking wave can produce as much energy loss as many small ones. Small breaking waves, however, occur much more frequently and thus their overall contribution to wave dissipation cannot be neglected. Extensive study is required of both breaking wave statistics, especially at smaller scales, and energy dissipation rate in individual breaking waves, so as to acquire a better estimate of total wave dissipation by breaking.

Acknowledgments. The instrument was developed by R. C. Teichrob, C. J. Elder, and D. G. Sieberg at the Institute of Ocean Sciences. Dr. Jerry Smith at the Scripps Institution of Oceanography kindly provided

the directional wave spectra. This work was supported by the U.S. Office of Naval Research and the Canadian Panel on Energy Research and Development. Li Ding was supported by a University of Victoria Fellowship.

APPENDIX A

Detection Probability

In the following analysis of detectability and breaking duration, the intensity of background noise will for simplicity be considered a constant rather than a random variable. This is based on the observation that the variability of noise intensity is much smaller than that of the intensity of individual events (Ding 1993). Therefore, when both are involved in the same problem, the randomness of noise intensity can be ignored.

Many experiments have suggested that the dipole pattern is a good assumption for the acoustic radiation of surface noise sources (Urick 1983). That is, the intensity at depth h for a breaking event located at range r is given by

$$I(r, h) = \frac{I_0 h^2}{(r^2 + h^2)^2}, \tag{A1}$$

with absorption neglected, where I_0 is the source intensity at 1 m distance on the beam axis ($r = 0$ and $h = 1$). It has also been suggested in Ding and Farmer (1992b) that I_0 can be assumed to be exponentially distributed,

$$f_{I_0}(I_0) = \frac{1}{\bar{I}_0} e^{-I_0/\bar{I}_0}. \tag{A2}$$

As a result, the distribution of the received intensity $I(r, h)$ is found from Eqs. (A1) and (A2) to be

$$f_I(I|r) = \frac{h^2}{\bar{I}_0}(1 + \eta^2)^2 \exp\left\{-\frac{Ih^2}{\bar{I}_0}(1 + \eta^2)^2\right\}, \tag{A3}$$

where $\eta = r/h$. Consequently, the detection probability of a breaking event at horizontal range r, is given by

$$p_D(z_d|r) = \int_{I_d}^{\infty} f_I(I|r)dI = \exp\{-z_d^2(1 + \eta^2)^2\}, \tag{A4}$$

where

$$z_d = \left(\frac{\bar{I}_d}{\bar{I}_0}\right)^{1/2} h$$

and I_d is the required detection intensity.

APPENDIX B

Maximum Likelihood Correction of Duration

The correction of breaking duration requires an assumption of the acoustical radiation process of breaking waves. That is, the received intensity should be expressed as a time-dependent function:

$$I(t) = Ip(t) = \frac{I_0 h^2}{(r^2 + h^2)^2} p(t). \tag{B1}$$

The choice of $p(t)$ is rather arbitrary due to lack of a priori information. We choose $p(t)$ to be a Hamming function for simplicity,

$$p(t) = \cos^2\left(\frac{\pi t}{T}\right) \quad -\frac{T}{2} \leqslant t \leqslant \frac{T}{2}, \tag{B2}$$

where T is the true duration of a breaking event. Under the circumstances, this choice appears reasonable while proving mathematically tractable. Further study is required to test the appropriateness of Eq. (B2) or derive an alternative and possibly more realistic time-dependent function.

Let I_d be the detection threshold as defined in appendix A. Then the measured duration $\hat{D} = 2t_d$ satisfies the relation

$$I_d = I \cos^2\left(\frac{\pi t_d}{T}\right),$$

from which we can find the distribution of t_d

$$f_d(t_d) = f_I\left[I_d \sec^2\left(\frac{\pi t_d}{T}\right)\right]\frac{dI}{dt_d}, \tag{B3}$$

where $f_I(\ \ )$ is given in Eq. (A3). The ML estimate of T can be found by choosing T to maximize $f_d(t_d)$, the solution of which is the root of

$$2\alpha^2 x \tan^2 x \sec^2 x - x(3 \tan^2 x + 1) - \tan x = 0, \tag{B4}$$

where

$$\alpha = z_d(1 + r^2/h^2), \quad x = \frac{\pi t_d}{T}.$$

Then

$$\hat{T}_{\mathrm{ML}} = \frac{\pi \hat{D}}{2\hat{x}_{\mathrm{ML}}}.$$

Note that the correction also depends on z_d. As discussed in appendix D, this may be affected by finite source dimension, but the effect is expected to be small.

APPENDIX C

Evaluation of the Effects of Background Noise

Assume that the position of breaking events (x, y) is uniformly distributed in an area of radius R, that is, the probability distribution of the position is given by

$$f(x, y) = \begin{cases} 1/\pi R^2, & x^2 + y^2 \leqslant R^2 \\ 0, & \text{otherwise.} \end{cases} \tag{C1}$$

Following the approach used to derive Eq. (A4), the detection probability for an event with intensity I_0 is found to be

$$p_D(I_0) = \int_{I_d}^{\infty} f_I(I|I_0)dI$$

$$= \begin{cases} 0, & I^* \leq z_d^2 \\ (h/R)^2(\sqrt{I^*}/z_d - 1), & \\ \qquad z_d^2 \leq I^* \leq z_d^2(1 + (R/h)^2)^2 & \\ 1, & I^* \geq z_d^2[1 + (R/h)^2]^2, \end{cases} \quad \text{(C2)}$$

where $I^* = I_0/\bar{I}_0$, and z_d and $\bar{I}_0$ are the same as defined in appendix A. The resulting I_0 distribution for detectable events in this area is, according to Bayers theorem (Papoulis 1984, p. 85), given by

$$f_D(I_0) = \frac{p_D(I_0)}{P_D} f_{I_0}(I_0), \quad \text{(C3)}$$

where $f_{I_0}(I_0)$ is the exponential distribution as given in Eq. (A2), and P_D is the total event detection probability:

$$P_D = \int_0^{\infty} p_D(I_0) f_{I_0}(I_0) dI_0.$$

As an example, $f_D(I_0)$ and $f_{I_0}(I_0)$ are shown in Fig. C1 against the normalized intensity I^* for dataset 3 in Table 1. While the exponential distribution decreases monotonically with I^*, the modified distribution shows a sharp increase at the beginning due to the background noise and starts to decrease monotonically at $I^* = 1$, which serves as a cutoff scale. The event duration and speed corresponding to this intensity scale depend on the relation between these parameters and the acoustic intensity. The only available information is the empirical relations described by Ding (1993), where the intensity of individual breaking waves was obtained from sound levels measured by the instrument and corrected for dipole radiation given their tracked position. The resulting intensity was scattered in relation to the measured event speed and duration, and a principle component analysis was thus applied to determine the relations. For dataset 3, these relations are

$$I_0 = 10^{8.4} V_e^{2.3}, \quad \text{(C4)}$$

$$I_0 = 10^{9.7} D_e^{2.0}, \quad \text{(C5)}$$

where V_e and D_e are event speed and duration (Ding 1993). The normalized variance of the data relative to Eqs. (C4) and (C5) are 0.62 and 0.52, respectively (the maximum variance is 1 when the data are completely uncorrelated).

Note that the above results were obtained for larger-scale breaking waves. Nevertheless, we may assume that they can be extrapolated down to smaller scales and then used to estimate the corresponding cutoff scales of duration and speed. To do so, we must first estimate the mean intensity $\bar{I}_0$. Equation (C2) implies that the minimum required intensity for a breaking wave to be detected is $I_{0\min} = \bar{I}_0 z_d^2$. For this dataset, $I_{0\min}$ and z_d are found to be 86 dB and 0.552, respectively (Ding 1993). Thus $\bar{I}_0$ is approximately 91 dB. Now using the relations in Eqs. (C4) and (C5), the corresponding cutoff scales of duration and speed are estimated to be of order 0.5 s and 1.8 m s^{-1}. Above these scales, the measured distribution still deviates from the true distribution, but the deviation in the mean scale is relatively small.[3] Note that these estimates are based on the empirical relations derived from larger-scale breaking waves, and only provide a rule of thumb for assessing the effect of background noise.

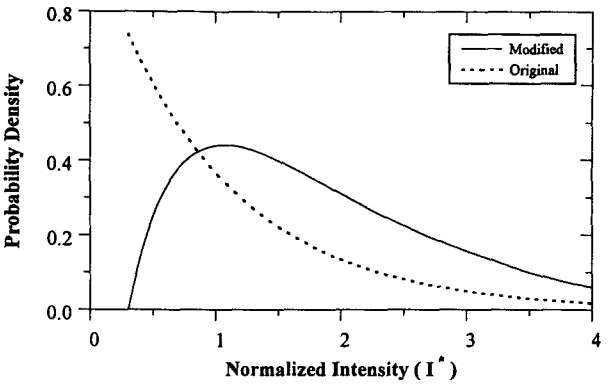

FIG. C1. Probability distribution of acoustic source intensity for detectable events, where the vertical axis is scaled by $\bar{I}_0$. The solid line is the modified distribution [$f_D(I_0)$], while the dashed line is the original (exponential) distribution for comparison (based on dataset 3 in the table).

APPENDIX D

Determination of Event Density

We notice that the detection probability in Eq. (A4) is dependent on z_d and the horizontal range, r. The range distribution of detected events will be determined only by z_d. Let $m(r)$ be the number of detected events in unit range interval at range r, and Q be the number of events per unit area. Then

$$m(r) = 2\pi r Q p_D(z_d|r),$$

where $p_D(z_d|r)$ is given in Eq. (A4). The total number of detected events is given by

$$N = \int_0^{\infty} m(r)dr = \frac{\sqrt{\pi}}{2} \pi Q h^2 \frac{1 - \text{erf}(z_d)}{z_d},$$

[3] The mean intensity of the detectable events for $I^* \geq 1$ (conditional mean) is about 14% greater than that of the total events. Thus, the corresponding mean event speed and duration of the detectable events are estimated to be approximately 6% greater than the true scales, based on Eqs. (C4) and (C5).

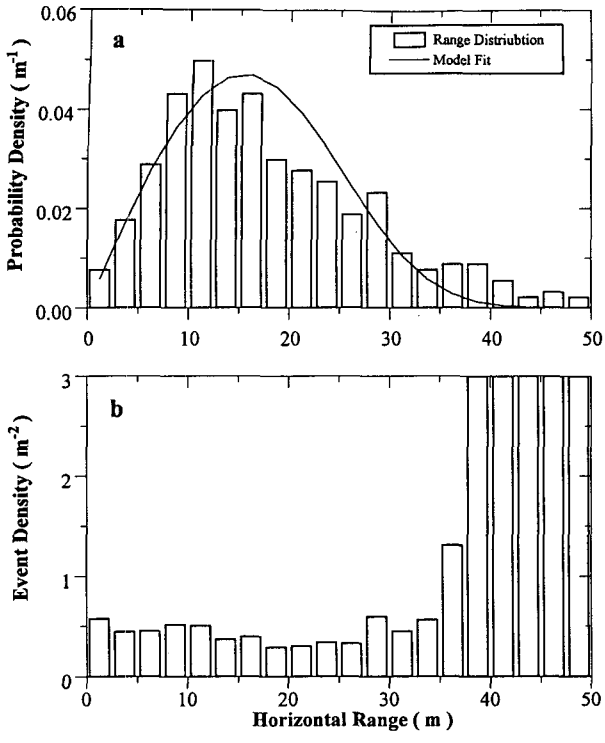

FIG. D1. Determination of event density. (a) Horizontal range distribution of events in a 30-min period, where the curve is the least-squares fit of the distribution. (b) Corrected event density in range from R_1 to $R_2 = R_1 + 2.5$ m. The flat region (0–35 m) is chosen to be the observation area, where event statistics are obtained.

where

$$\mathrm{erf}(x) = \frac{2}{\sqrt{\pi}} \int_0^x e^{-t^2} dt$$

is the error function. Then we obtain a normalized range distribution

$$n(r) = \frac{m(r)}{N}, \qquad \text{(D1)}$$

which depends only on z_d.

Figure D1a shows an observed normalized range distribution of locatable events for a period of 30 min (dataset 14). This distribution deviates from the distribution for detectable events since the number of events at shorter range may be reduced due to the finite source dimension effect. Generally speaking, the probability of loss due to finite source dimension decreases with increasing range. Nevertheless, the use of four independent hydrophone pairs improves the locatability of near events to an extent that depends on the event orientation (this factor is less important to farther events). Hence the distribution is not expected to be severely modified. [Moreover, z_d determined from the data using the following optimization scheme seems to be relatively insensitive to slight variations in $\hat{n}(r)$.] Therefore, we can choose z_d by best fitting $n(r)$ to the data, that is, by minimizing the cost function:

$$\text{cost} = \sum_i [n(r_i) - \hat{n}(r_i)]^2. \qquad \text{(D2)}$$

Once z_d is chosen, event density can be estimated from

$$\hat{Q} = \frac{\hat{N}(R_1, R_2)}{A_{\text{eff}} T_0}, \qquad \text{(D3)}$$

where $\hat{N}(R_1, R_2)$ is the number of detectable events located between horizontal range R_1 and R_2 during the period of T_0. The "effective" observation area A_{eff} is defined as

$$A_{\text{eff}} = \int_{R_1}^{R_2} 2\pi r p_D(z_d|r) dr$$

$$= \frac{\pi\sqrt{\pi}h^2}{2z_d} \{\Phi[z_d(1+\eta_2^2)] - \Phi[z_d(1+\eta_1^2)]\}, \qquad \text{(D4)}$$

where $\eta_1 = R_1/h$ and $\eta_2 = R_2/h$.

The curve in Fig. D1a gives the model distribution $n(r)$ in Eq. (D1), with z_d derived from the least-squares fit. Figure D1b shows the estimated density from Eq. (D3) as a function of R_1 and R_2. The flat region of Fig. 20b (0–35 m) is chosen to be the effective observation area. Event density is then averaged over this area by substituting $R_1 = 0$ and $R_2 = 35$ into Eqs. (D4) and (D3).

REFERENCES

Agrawal, Y. C., E. A. Terray, M. A. Donelan, P. A. Hwang, A. J. Williams III, W. M. Drennan, K. K. Kahma, and S. A. Kitaigorodskii, 1992: Enhanced dissipation of kinetic energy beneath surface waves. *Nature,* **359,** 219–220.

Bortkovskii, R. S., 1987: *Air–Sea Exchange of Heat and Moisture During Storms.* D. Reidel.

Crowther, P. A., and A. Hansla, 1993: The lifetimes, velocities, and probable origin of sonic and ultrasonic noise sources on the sea surface. *Natural Physical Sources of Underwater Sound,* B. Kerman, Ed., Kluwer Academic, 379–392.

Ding, L., 1993: Acoustical studies of breaking surface waves in the open ocean. Ph.D dissertation, University of Victoria, Victoria, B.C., Canada.

——, and D. M. Farmer, 1992a: A signal processing scheme for passive acoustical mapping of breaking surface waves. *J. Atmos. Oceanic Technol.,* **9,** 484–494.

——, and ——, 1992b: On the acoustical intensity of breaking waves. *Can. Acoust.,* **20,** 65–66.

Donelan, M., M. S. Longuet-Higgins, and J. S. Turner, 1972: Periodicity in whitecaps. *Nature,* **239,** 449–451.

Farmer, D. M., and S. Vagle, 1988: On the determination of breaking surface wave distribution. *J. Geophys. Res.,* **93**(C4), 3591–3600.

——, and L. Ding, 1992: Coherent acoustical radiation from breaking waves. *J. Acoust. Soc. Am.,* **92**(1), 397–402.

Hwang, P. A., D. Xu, and J. Wu, 1989: Breaking of wind-generated waves: Measurement and characteristics. *J. Fluid Mech.,* **202,** 177–200.

Longuet-Higgins, M. S., and M. J. H. Fox, 1977: Theory of the almost-highest wave: The inner solution. *J. Fluid Mech.,* **80,** 721–741.

——, and N. D. Smith, 1983: Measurements of breaking waves by a surface jump meter. *J. Geophys. Res.*, **88**(C14), 9823–9831.
Melville, W. K., 1994: Energy dissipation by breaking waves. *J. Phys. Oceanogr.*, **24,** in press.
——, and R. J. Rapp, 1985: Momentum flux in breaking waves. *Nature,* **317,** 514–516.
——, M. R. Loewen, F. C. Felizardo, A. T. Jessup, and M. J. Buckingham, 1988: The acoustic and microwave signatures of breaking waves. *Nature,* **336**(3), 54–56.
Monahan, E. C., and I. G. O'Muirheartaigh, 1986: Whitecaps and the passive remote sensing of the ocean surface. *Int. J. Remote Sens.*, **7,** 627–642.
Ochi, M. K., and C-H. Tsai, 1983: Prediction of occurrence of breaking waves in deep water. *J. Phys. Oceanogr.*, **13,** 2008–2019.
Papoulis, A., 1984: *Probability, Random Variables and Stochastic Processes.* 2d ed. McGraw-Hill.
Phillips, O. M., 1985: Spectral and statistical properties of the equilibrium range in wind-generated gravity waves. *J. Fluid Mech.*, **156,** 505–531.
——, and M. J. Banner, 1974: Wave breaking in the presence of wind drift and swell. *J. Fluid Mech.*, **66,** 625–640.
Snyder, R. L., and R. M. Kennedy, 1983: On the formation of whitecaps by a threshold mechanism. Part I: Basic formulation. *J. Phys. Oceanogr.*, **13,** 1482–1492.
——, L. Smith, and R. M. Kennedy, 1983: On the formation of whitecaps by a threshold mechanism. Part III: Field experiment and comparison with theory. *J. Phys. Oceanogr.*, **13,** 1505–1518.
Thorpe, S. A., 1992: Bubble clouds and the dynamics of the upper ocean. *Quart. J. Roy. Meteor. Soc.*, **118,** 1–22.
——, 1993: Energy loss by breaking waves. *J. Phys. Oceanogr.*, **23,** 2498–2502.
——, and P. N. Humpheries, 1980: Bubbles and breaking waves. *Nature,* **283,** 463–465.
——, and A. J. Hall, 1983: The characteristics of breaking waves, bubble clouds, and near-surface currents observed using side-scan sonar. *Contin. Shelf Res.*, **1,** 353–384.
Updegraff, G. E., and V. G. Anderson, 1991: Bubble noise and wavelet spills recorded at 1 m below the ocean surface. *J. Acoust. Soc. Am.*, **89,** 2264–2279.
Urick, J. R., 1983: *Principles of Underwater Sound.* 3d ed. McGraw-Hill.
Wu, J., 1979: Oceanic whitecaps and sea state. *J. Phys. Oceanogr.*, **9,** 1064–1068.
——, 1992: Individual characteristics of whitecaps and volumetric description of bubbles. *IEEE J. Oceanic Eng.*, **OE-17,** 150–158.
Zedel, L., and D. Farmer, 1994: Surface wave period modulations in near surface ambient sound. *J. Geophys. Res.*, in press.